

1 **A population of descending neurons that regulate the flight motor of *Drosophila***

2 Shigehiro Namiki^{1,3}, Ivo G. Ros², Carmen Morrow¹, William J. Rowell¹, Gwyneth M. Card^{*1},
3 Wyatt Korff^{*1}, Michael H. Dickinson^{*2,4}

4 ¹Janelia Research Campus, Howard Hughes Medical Institute, 19700 Helix Dr., Ashburn, VA
5 20147, USA

6 ²Division of Biology and Bioengineering, California Institute of Technology, 1200 E. California
7 Blvd., Pasadena CA, 91125, USA

8 ³The University of Tokyo, Research Center for Advanced Science and Technology, 4-6-1
9 Komaba, Meguro, Tokyo 153-8904, Japan

10 ⁴Lead Contact

11 *Authors for correspondence: cardg@janelia.hhmi.org, korffw@janelia.hhmi.org,
12 flyman@caltech.edu

13

14 **Summary**

15 Like many insect species, *Drosophila melanogaster* are capable of maintaining a stable flight
16 trajectory for periods lasting up to several hours(1, 2). Because aerodynamic torque is roughly
17 proportional to the fifth power of wing length(3), even small asymmetries in wing size require the
18 maintenance of subtle bilateral differences in flapping motion to maintain a stable path. Flies can
19 even fly straight after losing half of a wing, a feat they accomplish via very large, sustained
20 kinematic changes to the both damaged and intact wings(4). Thus, the neural network responsible
21 for stable flight must be capable of sustaining fine-scaled control over wing motion across a large
22 dynamic range. In this paper, we describe an unusual type of descending neurons (DNg02) that
23 project directly from visual output regions of the brain to the dorsal flight neuropil of the ventral
24 nerve cord. Unlike most descending neurons, which exist as single bilateral pairs with unique
25 morphology, there is a population of at least 15 DNg02 cell pairs with nearly identical shape. By
26 optogenetically activating different numbers of DNg02 cells, we demonstrate that these neurons
27 regulate wingbeat amplitude over a wide dynamic range via a population code. Using 2-photon
28 functional imaging, we show that DNg02 cells are responsive to visual motion during flight in a
29 manner that would make them well suited to continuously regulate bilateral changes in wing
30 kinematics. Collectively, we have identified a critical set of DNs that provide the sensitivity and
31 dynamic range required for flight control.

32

33 Results

34 Within a fly's nervous system, sensory information from the brain is conveyed to motor regions of
35 the ventral nerve cord (VNC) by several hundred pairs of descending neurons (DNs) that are
36 roughly stratified into a dorsal pathway that projects to flight motor neuropils and a ventral pathway
37 that project to leg neuromeres(5, 6) (Figure 1A, B). Whereas most of the DNs are single pairs of
38 bilateral cells with unique morphology, a small number of DNs constitute larger sets of
39 homomorphic neurons. To identify classes of DNs that might be involved in flight control, we
40 conducted an activation screen in which we expressed CsChrimson(7) in one GAL4 line and 48
41 split-GAL4 lines(8) that collectively target 29 different dorsally projecting DNs that innervate the
42 wing and haltere neuropils and tectulum of the VNC(6), along with one control split-GAL4 line that
43 does not drive expression in any neuron ("empty"). In each trial, we aligned tethered, flying flies
44 within a machine vision system to measure wingbeat amplitude(9). To promote stable flight during
45 each trial, we presented the flies with a pattern of vertical stripes presented on an LED array(10)
46 that covered 212° of their frontal field of view. While the flies regulated the angular velocity of the
47 visual pattern under closed-loop conditions, we presented a brief, 100 ms pulse of 617 nm light
48 to activate the targeted DNs (Fig. 1C, D). These 50 lines varied not only with respect to the cells
49 they labeled, but also the sparsity of expression. Nevertheless, a clear pattern emerged when
50 comparing the results across lines (Fig. 1E). Of the 13 lines in which CsChrimson activation
51 resulted in the largest change in wingbeat amplitude, 11 targeted members of the same class of
52 neurons, DN_g02.

53

54 The DN_g02s were previously identified anatomically(6) and consist of a cluster of at least 15 cell
55 pairs with nearly identical morphology, the largest of the population-type class of DN_s identified
56 so far. Their small, spindly cell bodies reside in a cluster at the ventral edge of the gnathal ganglion
57 (GNG; Figure 2A). The primary neurites of the DN_g02s run ventrally along the edge of the GNG
58 before taking a hairpin turn and ascending dorsally, where each cell arborizes in a hemi-circle
59 around the esophageal foramen. The cells' terminals reside within a set of five contiguous
60 neuropils consisting of the inferior bridge (IB), inferior clamp (ICL), superior posterior slopes
61 (SPS), inferior posterior slope (IPS), as well as the gnathal ganglion (GNG)(11). Synaptotagmin
62 labeling and fine morphology suggest that processes within the IB and GNG are outputs, whereas
63 those within the IC, SPS, and IPS are inputs(6).

64

65 After descending ipsilaterally down the neck connectives, the DN_g02 cells exhibit a distinct pattern
66 of arborization in the dorsal VNC (Figure 2B). Collectively, the population of cells forms a compact

67 'figure-of-eight' shape within the dorsal flight neuropil – a pattern also repeated in the haltere
68 neuropil (Figure 2F). Visualization of the morphology of individual neurons using the multi-color
69 flip out (MCFO) expression system(12) indicates that the arborizations of DN_g02s remain
70 restricted to the ipsilateral side within the brain, whereas the terminals in the VNC cross the
71 midsagittal plane (Figure 2A,B). Large synaptotagmin-positive boutons are distributed diffusely
72 throughout the projections in the wing and haltere neuropils (Figure 2C-E), consistent with output
73 synapses in these regions.

74

75 The large number of DN_g02 cells suggests that they might underlie some unique and critical
76 function within the flight motor system. One hypothesis is that the DN_g02s act on wing motion via
77 a population code(13, 14), such that the precise kinematic output of the wings depends in part on
78 the number of DN_g02 cells that are active as well as the level of activity within individual cells. To
79 test this hypothesis, we used 13 separate split-GAL4 lines that targeted different subsets of
80 DN_g02 cells with little or no expression in off-target neurons (Figure 2F). In addition, we evaluated
81 one GAL4 line (GMR42B02) that targets 15 DN_g02 cell pairs. As a control, we tested the empty
82 split-GAL4 line (SS03500). Because the number of DN_g02 cell pairs labeled in these 14 lines
83 varied from 0 to 15, we were able to test the influence of population activity by driving each line
84 independently and comparing the magnitude of the effect on wingbeat amplitude during flight. As
85 shown in Figure 3A, we found a strongly linear relationship ($r^2 = 0.7394$) between the number of
86 DN_g02 cells present in each line and the magnitude of the change in wingbeat amplitude elicited
87 by activation.

88

89 We further explored the effects of optogenetic activation on a subset of driver lines, focusing on
90 SS02625, a line that targets 8 DN_g02 cells (Figure 2F). Whereas individual flies varied with
91 respect to their background level of wingbeat amplitude prior to optogenetic activation (Figure 3B,
92 top traces), the peak level of wingbeat amplitude typically reached the same approximate value
93 for each fly during activation. This result suggests that the level of activation we applied elicited a
94 saturating excitation of the DN_g02 neurons within this line. In such cases, we also observed an
95 intriguing pattern of changes in wingbeat frequency elicited by the excitation (Figure 3B, bottom
96 traces). In most cases, DN_g02 activation resulted in a correlated rise in both wingbeat amplitude
97 and frequency, but in some instances the increase in amplitude was accompanied by a net
98 decrease in frequency. Whether activation elicited a decrease or increase in wingbeat frequency
99 was not random, but rather depended on the level of wingbeat frequency prior to activation. In
100 particular, individuals that flew with a lower wingbeat frequency exhibited a large increase in

101 frequency upon activation, whereas those that flew with a higher wingbeat frequency exhibited a
102 decrease (Figure 3C). A likely explanation for this peculiar trend emerges from plotting
103 instantaneous wingbeat frequency against wingbeat amplitude throughout the time course of
104 optogenetic activation for all the trials of an individual fly (Figure 3C). In each trial, CsChrimson
105 activation evoked an initial rapid rise in both wingbeat amplitude and frequency; however, once
106 the mean wingbeat amplitude of the two wings reached a value of about 160°, further increases
107 in amplitude were accompanied by a small decline in frequency (see also traces in bottom panel
108 of Figure 3B). Thus, when the DNg02 cells within the fly were maximally activated, we observed
109 an inverse relationship between wingbeat frequency and amplitude.

110
111 The time-varying relationship between wingbeat amplitude and frequency (Figure 3D) bear a
112 striking resemblance to data presented in a former study on the metabolic power requirements
113 for flight(15), in which changes in wingbeat amplitude and frequency were elicited by upward and
114 downward visual motion rather than optogenetic activation of DNs. That study presented a model
115 in which the mass specific mechanical power (\dot{P}_{mech}) delivered by the flight muscles sustains the
116 sum of induced power (the cost of lift) and profile power (the cost of drag) during flight. Profile
117 power, which is the dominant term, is proportional to the product of the wingbeat frequency and
118 amplitude cubed(3). Thus, their model predicts that when the mechanical power generated by the
119 flight muscles is constant—as it is when the asynchronous flight muscles are maximally
120 activated—any increase in wingbeat amplitude must be accompanied by a decrease in frequency
121 and vice versa. To analyze whether DNg02 activation may elicit near maximal power output, we
122 superimposed isolines for mechanical power in the frequency-amplitude plane, using equations
123 from the prior study(15). The precise values of these isolines are only approximate, because they
124 are based on average morphometric data for wing length, wing mass, and body mass of the flies
125 used in the prior study(15); we did not take those measurements on the flies used in our
126 experiments. However, the salient observation is that the set of amplitude-frequency values
127 elicited during peak DNg02 activation are bounded by the shape of the power isolines (e.g. $\dot{P}_{\text{mech}} \sim$
128 105 W kg^{-1}), which thus enforces the observed inverse relationship between wingbeat frequency
129 and wingbeat amplitude. These data suggest that optogenetic activation of this particular driver
130 line (SS02625) results in the production of peak mechanical power, presumably via activation of
131 the motor neurons of the large indirect flight muscles.

132
133 So far, our activation experiments suggest that the population of DNg02 cells might function
134 together to regulate flight power like a throttle, by controlling wingbeat amplitude in a bilateral

135 fashion via symmetric activation of power and steering muscle motor neurons. However, this
136 result may simply reflect the fact that optogenetic activation simultaneously excites both the left
137 and right DN_g02 cells in each fly. To test if left and right DN_g02 cells might operate independently during
138 steering maneuvers in flight, we performed 2-photon functional imaging from the dendritic region
139 of the neurons in one of the DN_g02 driver lines (SS02535) in tethered flying flies using GCaMP6f
140 as an activity indicator (Figure 4A). In preparing the flies for recording, we dissected a window in
141 the head capsule just dorsal to the esophageal foramen, which allowed us to image neurons on
142 the left and right side of the brain simultaneously (Figure 4B). Because our goal was to test
143 whether left and right DN_g02 cells might be active independently, we subjected the flies to an
144 array of different visual patterns during flight, chosen to elicit both symmetrical and asymmetrical
145 wingbeat responses. These stimulus epochs included a widefield pattern that moved upward or
146 downward, yaw motion to the left or right, a stripe oscillating on the left or right, roll motion to the
147 left or right, an expanding object on the left or right, progressive and regressive motion, and closed
148 loop stripe fixation (Figure 4C). The net results from this array of visual patterns was consistent
149 in that they demonstrated unequivocally that at least some DN_g02 cells can respond differently
150 on the left and right sides of the brain. This result was most apparent in yaw stimuli (Figure 4D,
151 left traces), during which rightward motion elicited an increase in activity of the right DN_g02 cells
152 and a simultaneous decrease in activity of the left DN_g02 cells (and vice versa for leftward
153 motion). The changes in cell fluorescence were accompanied by the expected asymmetric
154 changes in wingbeat amplitude for a yaw response. In contrast, bilaterally symmetrical visual
155 patterns, such as regressive visual motion, elicited synchronous changes in activity of the right
156 and left DN_g02 cells, accompanied by symmetrical changes in wingbeat amplitude (Figure 4D,
157 rightmost traces). These results indicate that the DN_g02 cells can operate independently on the
158 left and right side of the brain in an asymmetrical or symmetrical fashion, depending on the pattern
159 of visual input. Across all recordings, we measured a strong correlation between the DN_g02 cells
160 and the wingbeat amplitude of the contralateral wing, and a weaker anti-correlation with the
161 wingbeat amplitude of the ipsilateral wing (Figure 4E). These patterns were readily apparent in
162 individual recordings, in which we determined the correlation coefficient between changes in
163 fluorescence ($\Delta F/F$) and wingbeat amplitude for each pixel in the fluorescence image during a 20
164 second flight epoch (Figure 4F). A pixel pattern that corresponds to the arbor of the right DN_g02
165 cells was highly correlated with left wingbeat amplitude, whereas a pixel pattern corresponding to
166 the left DN_g02 cells was highly correlated with right wingbeat amplitude.

167

168

169 Discussion

170 Compared to birds, bats, and pterosaurs—the three other groups of organisms capable of
171 sustained active flight—a unique feature of insects is that their wings are novel structures that are
172 not modified from prior ambulatory appendages. Insects retained the six legs of their apterogote
173 ancestors, but added two pairs of more dorsally positioned wings(16). This evolutionary quirk has
174 profound consequences for the underlying neuroanatomy of the insect flight system. Within their
175 thoracic ganglia, the sensory-motor neuropil associated with the wings constitutes a thin, dorsal
176 layer sitting atop the larger ventral regions that control leg motion(6, 17, 18). Numerically,
177 however, there appear to be more DNs targeting the flight neuropil than targeting the leg
178 neuromeres(6). This is surprising, given the more ancient status of the leg motor system and the
179 importance of legs in so many essential behaviors. However, the relatively large number of flight
180 DNs may reflect the fact that control of flight requires greater motion precision because even
181 minute changes in wing motion have large consequences on the resulting aerodynamics(19). In
182 this paper, we describe a class of DNs in *Drosophila* (DNg02) that are unusual in that instead of
183 existing as a unique bilateral pair, they constitute a large homomorphic population. By
184 optogenetically driving different numbers of cells, we demonstrated that DNg02 cells can regulate
185 wingbeat amplitude over a wide dynamic range (Figure 3A) and can elicit maximum power output
186 from the flight motor (Figure 3D). Using 2-photon functional imaging, we also show that at least
187 some DNg02 cells are responsive to large field visual motion during flight in a manner that would
188 make them well suited for continuously regulating wing motion in response to both bilaterally
189 symmetrical and bilaterally asymmetrical patterns of optic flow (Figure 4D).

190
191 Straight flight in *Drosophila* is only possible due to the maintenance of subtle and constant bilateral
192 differences in wing motion, carefully regulated by feedback from sensory structures such as the
193 eyes(20, 21), antennae(22, 23), and halteres(24, 25). The control system necessary for straight
194 flight must permit the maintenance of very large, yet finely regulated, distortions of wing motion in
195 order to produce perfectly balanced forces and moments. One means of controlling fine-scaled
196 sensitivity over a large dynamic range is through the use of a population code with range
197 fractionation. The use of a population code to specify motor output is a general principle(14) that
198 has been observed in a wide array of species including leeches(26), crickets(27),
199 cockroaches(28), and monkeys(29). In dragonflies, 8 pairs of DNs—a group of cells roughly
200 comparable in number to the DNg02 cells—project to the flight neuropil and encode the direction
201 to small visual targets(30).

202

203 Although the DNg02 neurons are morphologically similar, we strongly suspect that the population
204 is not functionally homogeneous. To fly straight with perfect aerodynamic trim, an animal needs
205 to zero its angular velocity about the yaw, pitch, and roll axes, in addition to regulating its forward
206 flight speed, side slip, and elevation. Thus, if the DNg02 cells are the main means by which flies
207 achieve flight trim, one would expect that they would be organized into several functional
208 subpopulations, with each set of cells controlling a different degree of freedom of the flight motor
209 system. For example, one subpopulation of DNg02 cells might be primarily responsible for
210 regulating roll, while another is responsible for regulating pitch, and yet another regulates forward
211 thrust. Such subpopulations need not constitute exclusive sets, but rather might overlap in
212 function, collectively operating like a joystick to regulate flight pose. If this hypothesis is correct,
213 we would expect the DNg02 neurons to differ with respect to both upstream inputs from
214 directionally tuned visual interneurons as well as downstream outputs to power and steering
215 muscle motor neurons. Unfortunately, we could not distinguish individual cell types across the
216 different driver lines we used at the level of light-based microscopy. If DNg02 cells are further
217 stratified into subclasses, it is likely that each driver line targets a different mixture of cell types.
218 Indeed, the variation we observed in changes in wingbeat amplitude as a function of the number
219 of DNg02 cells activated (Figure 3E) might reflect this variation in the exact complement of cells
220 targeted by the different driver lines. Further, although one driver line (R42B02) targets 15 DNg02
221 neurons, it is likely that this number underestimates the size of the entire population, and we
222 speculate that there may be a small set of neurons dedicated to regulating each output degree of
223 freedom. Collectively, our results suggest that we have identified a critical component of the
224 sensory motor pathway for flight control in *Drosophila*, the precise organization of which is now
225 available for further study using a combination of genetic, physiological, and connectomic
226 approaches.

227

228

229 **ACKNOWLEDGMENTS**

230 A portion of this work was conducted as part of the Descending Interneuron Project Team at
231 Janelia Research Campus. We would like to thank the Janelia Visiting Science Program for
232 hosting MHD, Gudrun Ihrke and The Project Technical Resources group for assistance in
233 coordinating the screening, and the Janelia FlyCore assisted with animal preparations. Research
234 reported in this publication was supported by the Howard Hughes Medical Institute (S.N., W.J.R.,
235 G.M.C., W.K.) and the National Institute of Neurological Disorders and Stroke of the National
236 Institutes of Health (I.G.R., M.H.D.) under Award U19NS104655.

237

238 **AUTHOR**

CONTRIBUTIONS

239 (Following CRediT taxonomy): Conceptualization: S.N., G.M.C., W.K, and M.H.D.; Methodology:
240 S.N., G.M.C., W.K., and M.H.D.; Software: I.G.R., W.J.R.; Validation: W.J.R., C.M., W.K., G.M.C.,
241 I.G.R., M.H.D.; Formal Analysis: S.N., I.G.R., C.M., W.J.R., W.K., M.H.D.; Investigation: S.N.,
242 I.G.R., W.J.R.; Resources: G.M.C. W.K., M.H.D.; Data Curation: C.M., W.J.R., I.G.R.; Writing
243 (Original Draft): S.N., M.H.D.; Writing (Review & Editing): W.K., I.G.R., M.H.D.; Visualization:
244 S.N., I.G.R., C.M., W.K., M.H.D.; Funding Acquisition: G.M.C., W.K., M.H.D.; Supervision:
245 G.M.C., W.K., M.H.D.; Project Administration: G.M.C., W.K., M.H.D.

246

247 **DECLARATION OF INTERESTS**

248 The authors have no competing interest to declare.

249

250 **STAR METHODS**

251

252 **KEY RESOURCES TABLE**

REAGENT or RESOURCE	SOURCE	IDENTIFIER
Chemicals, Peptides, and Recombinant Proteins		
All-trans-retinal	Sigma-Aldrich	CAS: 116-31-4
Schneider's Insect Medium	Sigma-Aldrich	S0146
Triton X-100	Sigma-Aldrich	X100
Xylene	Thermo Fisher Scientific	x5-500
Dibutyl phthalate in xylene (DPX)	Electron Microscopy Sciences	13512
Paraformaldehyde	Electron Microscopy Sciences	15713-S
Antibodies		
Mouse mAb anti-Bruchpilot (nc82)	Developmental Studies Hybridoma Bank	nc82; RRID: AB_2314866
rabbit polyclonal anti-GFP	Thermo Fisher Scientific	Cat #: A-11122; RRID: AB_221569
Alexa Fluor 488 goat anti-rabbit	Thermo Fisher Scientific	Cat #: A-11034; RRID: AB_2576217
Alexa Fluor 568 goat anti-mouse	Thermo Fisher Scientific	Cat #: A-11031; RRID: AB_144696
Deposited Data		
Raw and analyzed data	This paper	https://doi.org/10.17632/7q984jm2zc.1
Experimental Models: Organisms/Strains		
<i>D. melanogaster</i> : UAS-CsChrimson	Bloomington Drosophila Stock Center	RRID:BDSC_55135
<i>D. melanogaster</i> : UAS-OpGCaMP6f (20XUAS-IVS-Syn21-OpGCamp6F-p10 in attP5)	Gift from D. Anderson	N/A
<i>D. melanogaster</i> : UAS-tdTomato (P{w[+mC]=UAS-tdTom.S}3)	Bloomington	RRID:BDSC_36328
<i>D. melanogaster</i> : UAS-OpGCaMP6f; UAS-tdTomato	Constructed from above two lines	N/A
<i>D. melanogaster</i> : pJFRC200-10XUASIVS- myr::smGFP-HA in attP18	[(31)]	N/A
<i>D. melanogaster</i> : SS01074	Bloomington Drosophila Stock Center	RRID:BDSC_75840
<i>D. melanogaster</i> : SS01063	Bloomington Drosophila Stock Center	RRID:BDSC_75837
<i>D. melanogaster</i> : SS00735	Bloomington Drosophila Stock Center	RRID:BDSC_75998

D. melanogaster: SS01540	Bloomington Drosophila Stock Center	RRID:BDSC_75903
D. melanogaster: SS01052	Bloomington Drosophila Stock Center	RRID:BDSC_75825
D. melanogaster: SS01558	Bloomington Drosophila Stock Center	RRID:BDSC_75946
D. melanogaster: SS02377	Bloomington Drosophila Stock Center	RRID:BDSC_75874
D. melanogaster: SS02384	Bloomington Drosophila Stock Center	RRID:BDSC_75958
D. melanogaster: SS01053	Bloomington Drosophila Stock Center	RRID:BDSC_86728
D. melanogaster: SS02631	Bloomington Drosophila Stock Center	RRID:BDSC_75976
D. melanogaster: SS02536	Bloomington Drosophila Stock Center	RRID:BDSC_75940
D. melanogaster: SS01069	Bloomington Drosophila Stock Center	RRID:BDSC_75828
D. melanogaster: SS02542	Bloomington Drosophila Stock Center	RRID:BDSC_75941
D. melanogaster: SS01546	Bloomington Drosophila Stock Center	RRID:BDSC_75944
D. melanogaster: SS02392	Bloomington Drosophila Stock Center	RRID:BDSC_75878
D. melanogaster: SS1075	Bloomington Drosophila Stock Center	RRID:BDSC_75841
D. melanogaster: SS01056	Bloomington Drosophila Stock Center	RRID:BDSC_75818
D. melanogaster: SS01556	Bloomington Drosophila Stock Center	RRID:BDSC_75953
D. melanogaster: SS02393	Bloomington Drosophila Stock Center	RRID:BDSC_75933
D. melanogaster: SS02608	Bloomington Drosophila Stock Center	RRID:BDSC_75966
D. melanogaster: SS01058	[(6)]	N/A
D. melanogaster: SS02383	Bloomington Drosophila Stock Center	RRID:BDSC_75888
D. melanogaster: SS02552	Bloomington Drosophila Stock Center	RRID:BDSC_75942

D. melanogaster: SS02379	Bloomington Drosophila Stock Center	RRID:BDSC_75963
D. melanogaster: SS02635	Bloomington Drosophila Stock Center	RRID:BDSC_75969
D. melanogaster: SS03500	This paper	N/A
D. melanogaster: SS02111	Bloomington Drosophila Stock Center	RRID:BDSC_75935
D. melanogaster: SS02396	Bloomington Drosophila Stock Center	RRID:BDSC_75882
D. melanogaster: SS01579	Bloomington Drosophila Stock Center	RRID:BDSC_75902
D. melanogaster: SS02634	Bloomington Drosophila Stock Center	RRID:BDSC_75970
D. melanogaster: SS02617	Bloomington Drosophila Stock Center	RRID:BDSC_75967
D. melanogaster: SS01061	Bloomington Drosophila Stock Center	RRID:BDSC_75836
D. melanogaster: SS02551	This paper	N/A
D. melanogaster: SS02553	Bloomington Drosophila Stock Center	RRID:BDSC_75936
D. melanogaster: SS02627	This paper	N/A
D. melanogaster: SS01049	Bloomington Drosophila Stock Center	RRID:BDSC_75833
D. melanogaster: SS01541	Bloomington Drosophila Stock Center	RRID:BDSC_75891
D. melanogaster: SS01577	This paper	N/A
D. melanogaster: SS01578	This paper	N/A
D. melanogaster: SS01560	Bloomington Drosophila Stock Center	RRID:BDSC_75948
D. melanogaster: SS02535	This paper	N/A
D. melanogaster: SS01073	Bloomington Drosophila Stock Center	RRID:BDSC_75839
D. melanogaster: SS02625	Bloomington Drosophila Stock Center	RRID:BDSC_75974
D. melanogaster: SS01563	This paper	N/A

D. melanogaster: SS02630	This paper	N/A
D. melanogaster: SS02550	This paper	N/A
D. melanogaster: SS01562	This paper	N/A
D. melanogaster: GMR42B02	Bloomington Drosophila Stock Center	RRID:BDSC_68782
D. melanogaster: SS02624	Bloomington Drosophila Stock Center	RRID:BDSC_75972
D. melanogaster: SS02544	This paper	N/A
Software and Algorithms		
Kinefly wing tracking software	[(9)]	https://github.com/ssafarik/Kinefly
Python	https://www.python.org	RRID: SCR_008394
Matplotlib	https://matplotlib.org	RRID: SCR_008624
MATLAB	https://www.mathworks.com	RRID: SCR_001622
FIJI	https://fiji.sc/	RRID:SCR_002285
Other		
UV-activated cement	Henkel	Loctite® 3972TM
Digital camera	Balser	acA640–120 gm
Long-pass filter	Midwest Optical Systems	LP715-30.5
Fiber optic light guide	Thorlabs	FT1500EMT
IR light source LED	Thorlabs	M850F2
IR light source driver	Thorlabs	LEDD1B
Wingbeat analyzer	Phidgets	PhidgetAnalog 1002
Data acquisition system	Axon Instruments	Digitata 1440A
Panel controller	IO Rodeo	Panels display controller unit
Transmission filter	Indigo	Roscolux no. 59 filter
Transmission filter	Skelton Exotic Sangria	Rosco no. 39 filter
Transmission filter	Cyan	Rosco #4390 filter

253

254

255 **RESOURCE AVAILABILITY**

256

257 **Lead contact**

258 Further information and requests for resources and reagents should be directed to and will be
259 fulfilled by the Lead Contact, Michael H. Dickinson (flyman@caltech.edu).

260

261 **Materials availability**

262 All new fly lines generated for this paper are listed in the key resources table.

263

264 **Data and code availability**

265 All data has been deposited on Mendeley at <https://doi.org/10.17632/7q984jm2zc.1> and are
266 publicly available as of the date of publication. The DOI is listed in the key resources table. All
267 original code for data analysis has been deposited on Mendeley at
268 <https://doi.org/10.17632/7q984jm2zc.1> and is publicly available as of the date of publication. All
269 original code used for the kinefly wing tracking software is publicly available on Github at
270 <https://github.com/ssafarik/Kinefly>. The DOIs are listed in the key resources table. Any additional
271 information required to reanalyze the data reported in this paper is available from the lead contact
272 upon request.

273

274 **EXPERIMENTAL MODEL AND SUBJECT DETAILS**

275 All experiments were conducted on genetically modified female *Drosophila melanogaster*. To
276 create genetic lines that specifically targeted DNg02 cells, we used the split-GAL4 technique
277 described previously (Luan et al. 2006; Namiki et al. 2018). We combined split half lines that have
278 promoters to drive expression of either the transcription activation domain (p65ADZp) or the DNA-
279 binding domain (ZpGAL4DBD) of the GAL4 protein. To identify driver lines containing DNg02, we
280 manually searched the brain expression pattern from publically available GAL4 lines in the
281 FlyLight database (<https://flweb.janelia.org/>). We chose pairs of these driver lines that appeared
282 to target the DNg02 cells and screened the resulting split-GAL4 combinations by crossing them
283 with flies carrying the reporter pJFRC200-10XUASIVS-myr::smGFP-HA inserted into attP18. For
284 the optogenetic activation experiments, we used 3-to-6-day-old female flies obtained by crossing
285 virgin females from each split-GAL4 line (or GMR42B02) with 3-to-5-day-old males carrying
286 20XUAS-CsChrimson-mVenus inserted into attP18. We reared the progeny of this cross on
287 standard cornmeal fly food containing 0.2 mM all trans-Retinal (ATR) (Sigma-Aldrich) and
288 transferred adult flies 0-2 days after eclosion onto standard cornmeal fly food with 0.4 mM ATR.

289 We supplemented the standard cornmeal food with additional yeast. For functional imaging
290 experiments, we used 2-5 days old female flies that resulted from a cross of the split-GAL4 line
291 SS02535 with w+;UAS-tdTomato;UAS-GCaMP6f flies(32).

292

293 **QUANTIFICATION AND STATISTICAL ANALYSIS**

294 All experiments were analyzed with custom written scripts written in either Matlab or Python. This
295 manuscript includes no explicit tests of significance. Sample sizes refer to the number of
296 individuals tested.

297

298 **METHODS DETAILS**

299

300 **Optogenetic activation experiments**

301 Female offspring of split-GAL4 driver lines crossed to flies carrying 20XUAS-CsChrimson-
302 mVenus were anesthetized on a cold surface (4°C) and tethered to a tungsten pin with Loctite®
303 3972™ UV-activated cement (Henkel). The tethered fly was positioned such that its stroke plane
304 was horizontal and perpendicular to the vertical optical axis of a digital camera (Basler acA640–
305 120 gm) equipped with an Infinistix 90-degree lens with a long-pass filter (LP715-30.5, Midwest
306 Optical Systems). Two horizontally oriented fiber optic light guides (FT1500EMT; Thorlabs), each
307 coupled to an IR light source (driver: LEDD1B, and LED: M850F2; Thorlabs) illuminated the stroke
308 planes of the left and right wings. We used Kinefly software(9) to track the anterior-most angular
309 excursion of the fly's left and right wingbeat (Figure 1C). Digital values for the left and right
310 wingbeat amplitudes were converted into voltages using a PhidgetAnalog 1002 (Phidgets), and
311 recorded on a Digitata 1440A data acquisition system (Axon Instruments) for subsequent
312 analysis. The voltage signals from the two wings were also sent to an LED panel controller(10)
313 (IOrodeo) which was programmed so that flies could regulate the angular velocity of the visual
314 display via the difference in wingbeat amplitude of the two wings. We used a custom-built
315 photodetector circuit to record the oscillations in the incident IR light caused by the flapping motion
316 of the wings and convert that signal into a voltage proportional to wingbeat frequency
317 (https://github.com/janelia-kicad/light_sensor_boards), which we also recorded on the Digidata
318 1440A. For optogenetic activation, we positioned a fiber optic light guide (FT1500EMT; Thorlabs)
319 beneath the fly, aimed at the thorax, which conducted the output of a 617 nm LED (M617F1,
320 Thorlabs) at ~3.4 mW/mm². The timing and duration of the pulse was controlled via the voltage
321 input to the LED driver (LEDD1B, Thorlabs). The fly and ancillary instruments were surrounded
322 by a 12 x 4 panel (96 x 32 pixel) LED arena (470 nm)(10) that covered 216° of azimuth with a

323 resolution of 2.25° in front of the fly. In each experiment, we elicited 30 responses to a 100 ms
324 light pulse with an interpulse interval of 10 seconds under visual closed loop conditions, in which
325 the difference in fly's left-right wingbeat amplitude controlled the angular velocity of a striped drum
326 with a spatial frequency of 36°. For each trial, we determined the average wingbeat amplitude
327 (WBA) of the left and right wings over the 0.5 second period prior to stimulus onset and subtracted
328 this value from the entire trace to create a zero baseline. The response to optogenetic activation
329 was calculated as the average value of WBA over the 0.5 second period starting with stimulus
330 onset. The 30 trails from each fly were averaged to create a single measurement for each
331 individual.

332

333 **Anatomy**

334 To image expression patterns, we dissected the complete central nervous systems of 3-to-5-day-
335 old female adult progeny in Schneider's Insect Medium (Sigma), fixed them in paraformaldehyde,
336 and then transferred them to a goat serum blocking buffer for 1 hr. We then replaced the buffer
337 with the primary antibodies (mouse nc82 supernatant at 1:30, rabbit polyclonal anti-GFP at
338 1:1000) diluted in phosphate buffered saline with 0.5% Triton X-100 (PBT) and gently agitated
339 the preparations for 36–48 hr at 4°C. After washing with PBT, the samples were then incubated
340 with secondary antibodies (Alexa Fluor 488 goat anti-rabbit, and Alexa Fluor 568 goat anti-mouse
341 at 1:400) diluted in PBT and agitated again at 4°C for 3 days. The samples were then washed,
342 fixed again in paraformaldehyde, mounted on a poly-L-lysine cover slip, cleared with xylene, and
343 embedded in dibutyl phthalate in xylene (DPX) on a microscope slide with spacers. After drying
344 for two days, samples were imaged at either 20X or 40X with a confocal microscope (Zeiss LSM
345 510) (Dionne et al. 2018). To discriminate the morphology of individual DN_g02 cells, we used a
346 multi-color flip out technique(12). To identify pre-synaptic terminal of DN_g02, we examined
347 neuronal polarity using a reporter (pJFRC51-3xUAS-Syt::smGFP-HA in su(Hw)attPa) that labels
348 synaptotagmin, a synaptic vesicle-specific protein. More detailed descriptions of these protocols
349 are available on the Janelia FlyLight website ([https://www.janelia.org/project-](https://www.janelia.org/project-team/flylight/protocols)
350 [team/flylight/protocols](https://www.janelia.org/project-team/flylight/protocols)). All images are available through the FlyLight Split-GAL4 website
351 (<https://splitgal4.janelia.org/cgi-bin/splitgal4.cgi>).

352

353 **Functional Imaging**

354 Tethered, flying flies were imaged at an excitation wavelength of 930 nm using a galvanometric
355 scan mirror-based two-photon microscope (Thorlabs) equipped with a Nikon CFI apochromatic,
356 near-infrared objective water-immersion lens (40x mag., 0.8 N.A., 3.5 mm W.D.). We used the 2-

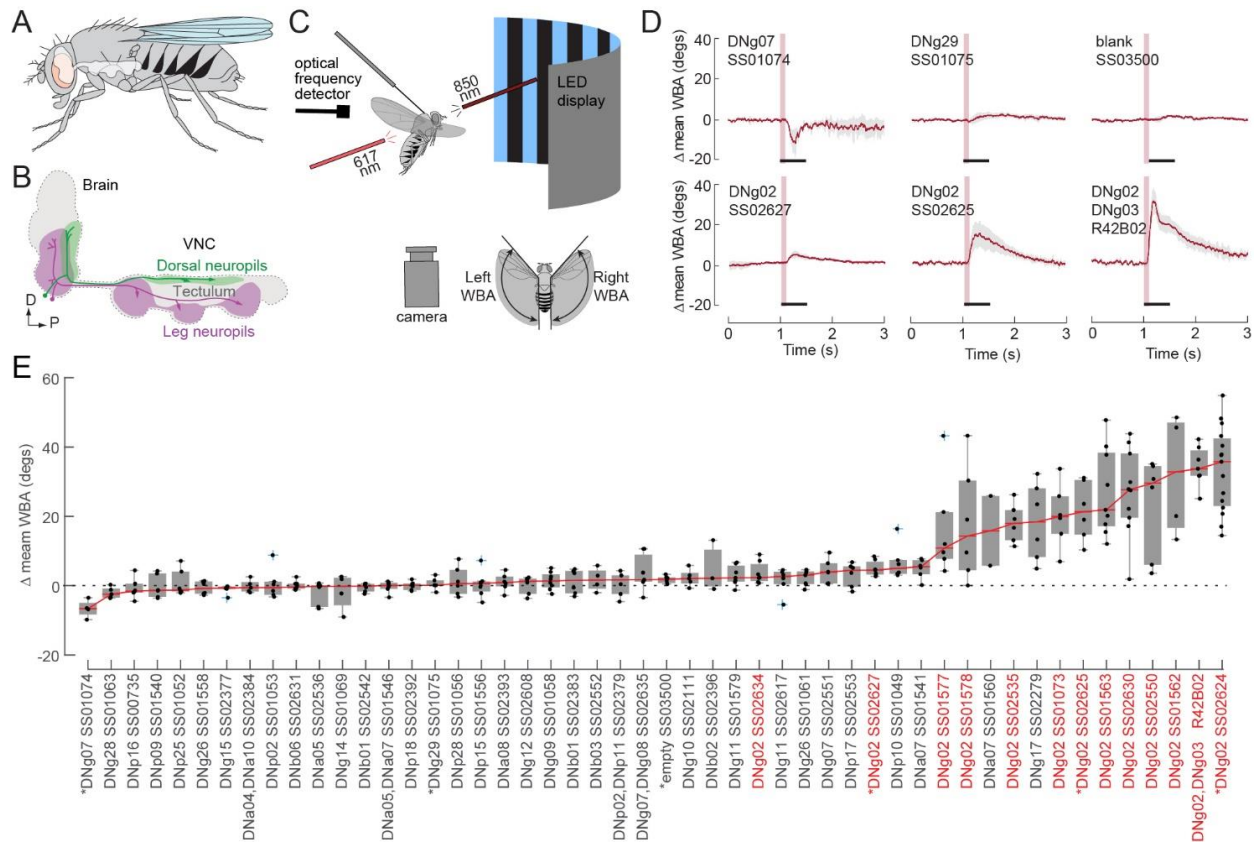
357 5 days old female progeny of a cross between the split-GAL4 driver line SS02535, which drives
358 expression in 3 pairs of DNg02s and $w^+;UAS\text{-}tdTomato;UAS\text{-}GCaMP6f$ flies(32). We recorded
359 two channels to image tdTomato and GCaMP6f fluorescence in the posterior slope arbors of both
360 left and right DNg02 neurons. Depending on the individual preparation, we acquired either 72 x
361 36 μm images with 128 x 64 pixel resolution at 13.1 Hz, or 72 x 29 μm images with 160 x 64 pixel
362 resolution at 11.2 Hz. To correct for horizontal motion in the x-y plane, we registered both
363 channels for each frame by finding the peak of the cross correlation between each tdTomato
364 image and the trial-averaged image(33). Based on tdTomato expression we selected a field of
365 view (FOV) approximately centered along the medio-lateral axis. The 20% most variable pixels in
366 the left and right halves of the GCaMP6f images were selected as the left and right regions of
367 interest (ROIs) respectively. To correct for motion in z, we normalized the GCaMP6f fluorescence
368 to the tdTomato fluorescence. For each frame and each side, we computed fluorescence (F_t) of
369 the GCaMP6f signal by subtracting the average of the background from the average of the ROI.
370 The background was defined as the 20% dimmest pixels of the entire FOV. We computed the
371 baseline fluorescence, F_0 , as the mean of the 10% lowest F_t in the ROI. To standardize the
372 measured neuronal activity across individual preparations we normalized baseline-subtracted
373 fluorescence to the maximum observed for each individual fly on each anatomical side of the brain
374 as $\Delta F/F = (F_t - F_0) / (F_t - F_0)_{\text{max}}$. We presented visual stimuli with a 12 x 4 panel (96 x 32 pixel)
375 arena that covered 216° of azimuth with a resolution of 2.25°, identical to that used in the
376 optogenetic screen. To reduce light pollution from the LED arena into the photomultiplier tubes of
377 the 2-photon microscope, we shifted the spectral peak of the visual stimuli from 470 nm to 450
378 nm by placing five transmission filters in front of the LEDs (one sheet of Roscolux no. 59 Indigo,
379 two sheets of no. 39 Skelton Exotic Sangria, and two sheets of no. 4390 Cyan). We presented an
380 array of visual patterns, each for 3 s, alternated with 3 s static starfields. The visual patterns were
381 presented in a shuffled pseudo-random order and included roll, pitch, and yaw motion in both
382 directions, a stripe oscillating on the left or right, an expanding object on the left or right,
383 progressive and regressive motion, and closed loop stripe fixation. We illuminated the wings using
384 four horizontal fiber-optic IR light sources (M850F2, Thorlabs) distributed in a ~90° arc behind the
385 fly. We tracked left and right wingbeat amplitudes with a machine vision system, Kinefly(9), at 32
386 Hz. This method introduces a delay in measurement of ~30 ms, which we corrected.
387

388 **References**

- 389 1. K. G. Götz, Course-control, metabolism and wing interference during ultralong tethered
390 flight in *Drosophila melanogaster*. *Journal of Experimental Biology* **128**, 35–46 (1987).
- 391 2. K. J. Leitch, F. V. Ponce, W. B. Dickson, F. van Breugel, M. H. Dickinson, The long-
392 distance flight behavior of *Drosophila* supports an agent-based model for wind-assisted
393 dispersal in insects. *PNAS* **118** (2021).
- 394 3. C. P. Ellington, The aerodynamics of hovering insect flight. VI. Lift and power
395 requirements. *Philosophical Transactions of the Royal Society of London. B, Biological*
396 *Sciences* **305**, 145–181 (1984).
- 397 4. F. T. Muijres, N. A. Iwasaki, M. J. Elzinga, J. M. Melis, M. H. Dickinson, Flies compensate
398 for unilateral wing damage through modular adjustments of wing and body kinematics.
399 *Interface Focus* **7**, 20160103 (2017).
- 400 5. C. T. Hsu, V. Bhandawat, Organization of descending neurons in *Drosophila*
401 *melanogaster*. *Sci Rep* **6**, 20259 (2016).
- 402 6. S. Namiki, M. H. Dickinson, A. M. Wong, W. Korff, G. M. Card, The functional organization
403 of descending sensory-motor pathways in *Drosophila*. *eLife* **7**, e34272 (2018).
- 404 7. N. C. Klapoetke, *et al.*, Independent optical excitation of distinct neural populations. *Nat*
405 *Methods* **11**, 338–346 (2014).
- 406 8. H. Luan, N. C. Peabody, C. R. Vinson, B. H. White, Refined Spatial Manipulation of
407 Neuronal Function by Combinatorial Restriction of Transgene Expression. *Neuron* **52**,
408 425–436 (2006).
- 409 9. M. P. Suver, A. Huda, N. Iwasaki, S. Safarik, M. H. Dickinson, An Array of Descending
410 Visual Interneurons Encoding Self-Motion in *Drosophila*. *J. Neurosci.* **36**, 11768–11780
411 (2016).
- 412 10. M. B. Reiser, M. H. Dickinson, A modular display system for insect behavioral
413 neuroscience. *Journal of Neuroscience Methods* **167**, 127–139 (2008).
- 414 11. K. Ito, *et al.*, A Systematic Nomenclature for the Insect Brain. *Neuron* **81**, 755–765 (2014).
- 415 12. A. Nern, B. D. Pfeiffer, G. M. Rubin, Optimized tools for multicolor stochastic labeling
416 reveal diverse stereotyped cell arrangements in the fly visual system. *PNAS* **112**, E2967–
417 E2976 (2015).
- 418 13. A. P. Georgopoulos, R. Caminiti, J. F. Kalaska, J. T. Massey, Spatial coding of movement:
419 A hypothesis concerning the coding of movement direction by motor cortical populations.
420 *EXP. BRAIN RES.* **49**, 327–336 (1983).
- 421 14. J. L. van Hemmen, A. B. Schwartz, Population vector code: a geometric universal as
422 actuator. *Biol Cybern* **98**, 509–518 (2008).

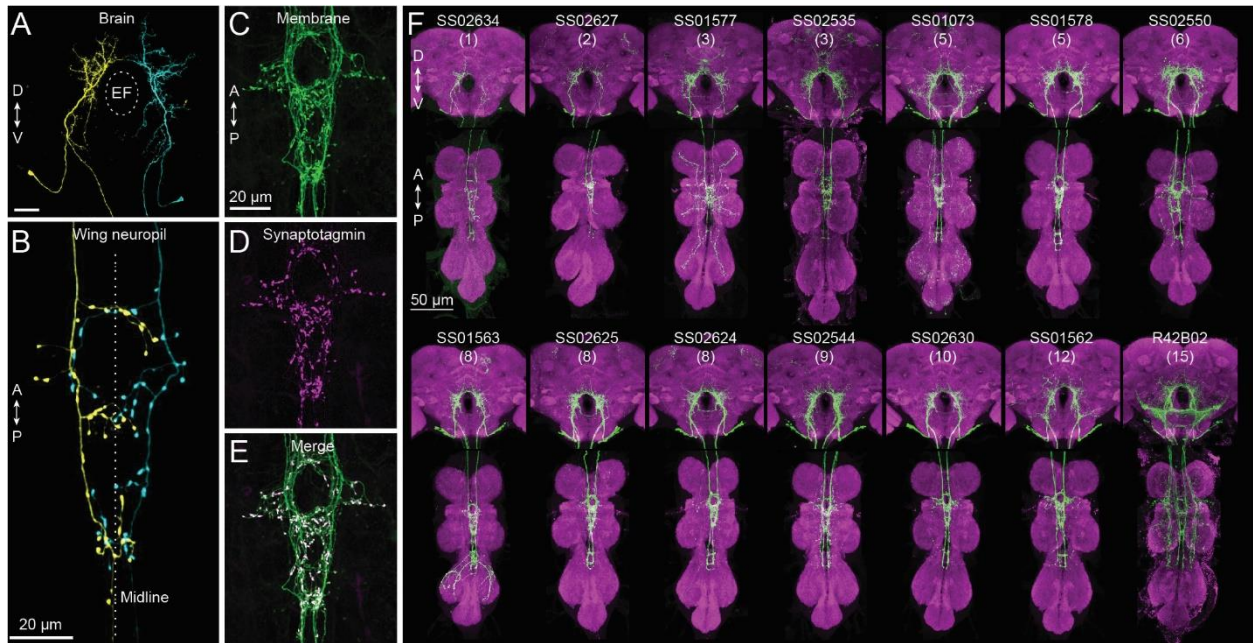
- 423 15. F. O. Lehmann, M. H. Dickinson, The changes in power requirements and muscle
424 efficiency during elevated force production in the fruit fly *Drosophila melanogaster*. *Journal*
425 *of Experimental Biology* **200**, 1133–1143 (1997).
- 426 16. J. Prokop, *et al.*, Paleozoic Nymphal Wing Pads Support Dual Model of Insect Wing
427 Origins. *Current Biology* **27**, 263–269 (2017).
- 428 17. N. J. Strausfeld, J.-K. Lee, Neuronal basis for parallel visual processing in the fly. *Visual*
429 *Neuroscience* **7**, 13–33 (1991).
- 430 18. R. Court, *et al.*, A Systematic Nomenclature for the *Drosophila* Ventral Nerve Cord. *Neuron*
431 **107**, 1071-1079.e2 (2020).
- 432 19. F. T. Muijres, M. J. Elzinga, J. M. Melis, M. H. Dickinson, Flies Evade Looming Targets by
433 Executing Rapid Visually Directed Banked Turns. *Science* **344**, 172–177 (2014).
- 434 20. K. G. Götz, Flight control in *Drosophila* by visual perception of motion. *Kybernetik* **4**, 199–
435 208 (1968).
- 436 21. J. Blondeau, M. Heisenberg, The three-dimensional optomotor torque system of *Drosophila*
437 *melanogaster*. *J. Comp. Physiol.* **145**, 321–329 (1982).
- 438 22. S. A. Budick, M. B. Reiser, M. H. Dickinson, The role of visual and mechanosensory cues
439 in structuring forward flight in *Drosophila melanogaster*. *Journal of Experimental Biology*
440 **210**, 4092–4103 (2007).
- 441 23. S. B. Fuller, A. D. Straw, M. Y. Peek, R. M. Murray, M. H. Dickinson, Flying *Drosophila*
442 stabilize their vision-based velocity controller by sensing wind with their antennae. *PNAS*
443 **111**, E1182–E1191 (2014).
- 444 24. L. Ristroph, *et al.*, Discovering the flight autostabilizer of fruit flies by inducing aerial
445 stumbles. *PNAS* **107**, 4820–4824 (2010).
- 446 25. M. H. Dickinson, Haltere-mediated equilibrium reflexes of the fruit fly, *Drosophila*
447 *melanogaster*. *Philosophical Transactions of the Royal Society of London. Series B:*
448 *Biological Sciences* **354**, 903–916 (1999).
- 449 26. J. E. Lewis, W. B. Kristan, A neuronal network for computing population vectors in the
450 leech. *Nature* **391**, 76–79 (1998).
- 451 27. O. Yono, T. Shimozawa, Synchronous firing by specific pairs of cercal giant interneurons in
452 crickets encodes wind direction. *Biosystems* **93**, 218–225 (2008).
- 453 28. R. Levi, J. M. Camhi, Population Vector Coding by the Giant Interneurons of the
454 Cockroach. *J. Neurosci.* **20**, 3822–3829 (2000).
- 455 29. A. P. Georgopoulos, A. B. Schwartz, R. E. Kettner, Neuronal population coding of
456 movement direction. *Science* **233**, 1416–1419 (1986).

- 457 30. P. T. Gonzalez-Bellido, H. Peng, J. Yang, A. P. Georgopoulos, R. M. Olberg, Eight pairs of
458 descending visual neurons in the dragonfly give wing motor centers accurate population
459 vector of prey direction. *PNAS* **110**, 696–701 (2013).
- 460 31. Y. Aso, *et al.*, The neuronal architecture of the mushroom body provides a logic for
461 associative learning. *eLife* **3**, e04577 (2014).
- 462 32. P. T. Weir, M. H. Dickinson, Functional divisions for visual processing in the central brain
463 of flying *Drosophila*. *PNAS* **112**, E5523–E5532 (2015).
- 464 33. M. Guizar-Sicairos, S. T. Thurman, J. R. Fienup, Efficient subpixel image registration
465 algorithms. *Opt. Lett.*, *OL* **33**, 156–158 (2008).
- 466



467

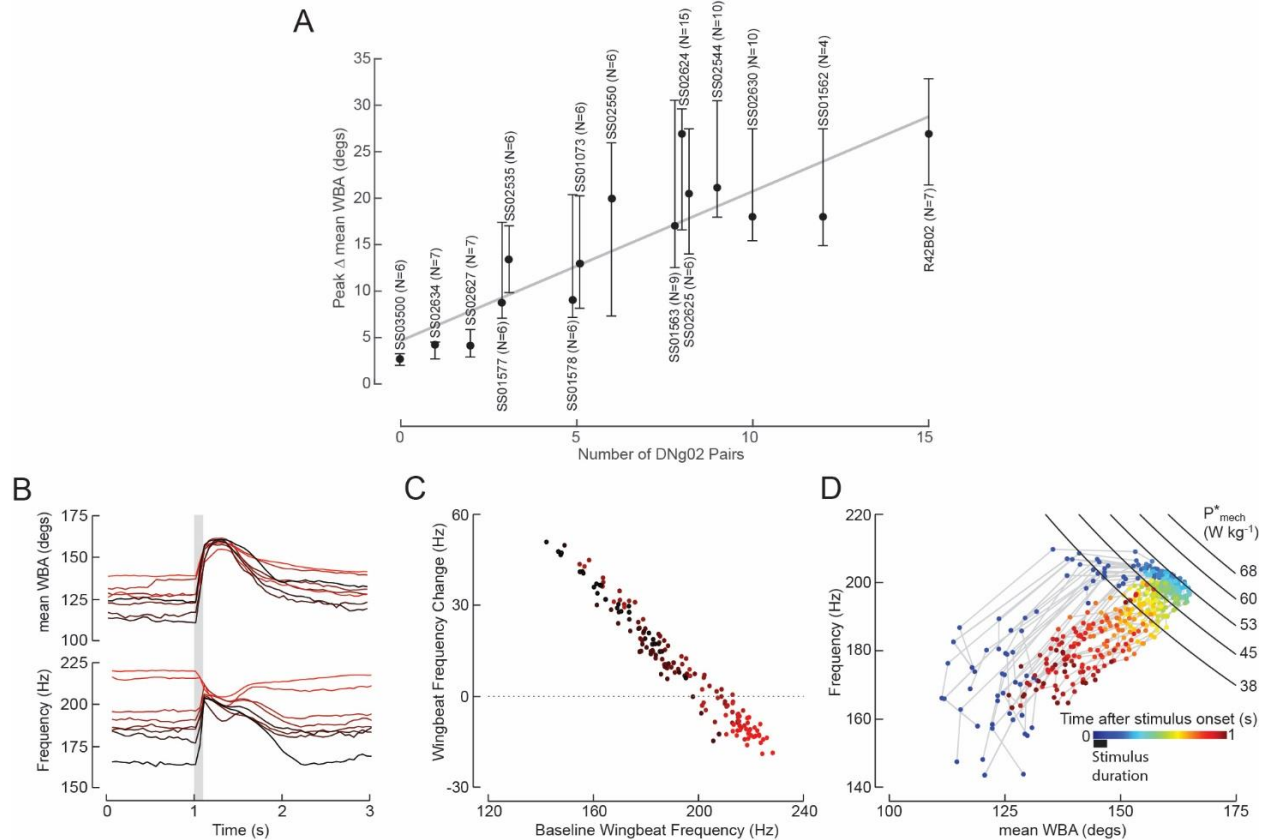
468 **Figure 1. Experimental methods for optogenetic activation and screen results.** (A) Cartoon showing location of
 469 central nervous system in a standing fly. (B) Descending neurons (DNs) are stratified into two main groups: a ventral
 470 group (magenta) that innervates the three leg neuromeres and a dorsal group (green) that innervates the dorsal
 471 neuropils associated with the neck, wings, and halteres. (C) Cartoon showing experimental set-up (not drawn to scale).
 472 A fiber optic cable delivering 617 nm light is positioned behind a tethered fly aimed at the thorax. Two fiber optic cables
 473 (only one is shown) deliver continuous near-IR light (850 nm) to illuminate the left and right stroke planes of the fly. The
 474 fly is centered within a curved visual display of blue (470 nm) LEDs upon which a striped drum (spatial frequency =
 475 36°) was presented under closed-loop conditions. An image of the fly is captured with an upward facing camera and
 476 analyzed using a real-time machine vision system that measures the angular extent of the left and right wingbeat
 477 amplitudes. In all experiments, we assumed that the rearward reversal angle was parallel to the body axis and remained
 478 constant. An optical detector that recorded fluctuations in IR light was used to record wingbeat frequency. (D) Results
 479 of 100 ms pulses of CsChrimson activation on the change in the mean of the left and right wingbeat amplitude of the
 480 wings in 6 of the 50 lines tested; red line and gray area indicate the mean response and the standard deviation
 481 envelope, respectively. One line (SS01074), which targets the DNg07 neuron, was distinct in that it elicited a consistent
 482 decrease in wingbeat amplitude. Most targeted cells, such as the DNg29 neuron shown in Figure 1 (labeled by
 483 SS01075) did not elicit a detectable change in wingbeat amplitude. Control flies in which the UAS-CsChrimson line
 484 was crossed with an empty vector split-GAL4 line (blank, SS03500) exhibited no response to the 617 nm light. Bottom row:
 485 Example traces of different driver lines that target the DNg02 cells. For each trial, we determined the average wingbeat
 486 amplitude (WBA) of the left and right wings over the 0.5 second period prior to stimulus onset and subtracted this value
 487 from the entire trace to create a zero baseline. The response to optogenetic activation was calculated as the average
 488 value of WBA over the 0.5 second period starting with stimulus onset. (E) Overview of the entire screen of 50 lines,
 489 ranked from left to right according to the magnitude of the optogenetic effect on wingbeat amplitude. Each trial
 490 was scored by averaging the change in the mean of wingbeat amplitude over the 500 ms period beginning with the
 491 onset of the light pulse (indicated by black bars in B). For each line, the median response is indicated by a red line.
 492 The median value from each individual fly is indicated by a black dot, the box and whisker plots indicate the
 493 interquartile range and extreme values for the flies tested; outliers are indicated by blue crosses. Lines that target
 494 DNg02 neurons are indicated by red font. Asterisks indicate lines for which the responses are plotted in panel D.



495

496 **Figure 2. Morphology of DNg02 cells and split-GAL4 driver lines targeting different numbers of neurons.** (A)
497 MCFO of SS02627 driver line showing one left and one right DNg02 neuron in the brain; approximate position of
498 esophageal foramen (EF) is indicated by dotted ellipse. (B) Projections of the same neurons in the wing neuropil. The
499 neurons possess punctate terminals on both sides of the VNC midline. (C) Enlarged view of wing neuropil region of
500 SS01578 showing GFP expression in green. (D) Same region as in B, showing synaptotagmin staining in magenta. (E)
501 Merger of images from B and C; DNg02 projections in the wing neuropil contain many output terminals. (F) Expression
502 pattern in 14 different driver lines that target DNg02 neurons. Membrane-targeted GFP expression is shown in green,
503 nc82 staining is shown in magenta. The number of neurons targeted in each line is shown in parenthesis below the line
504 name.

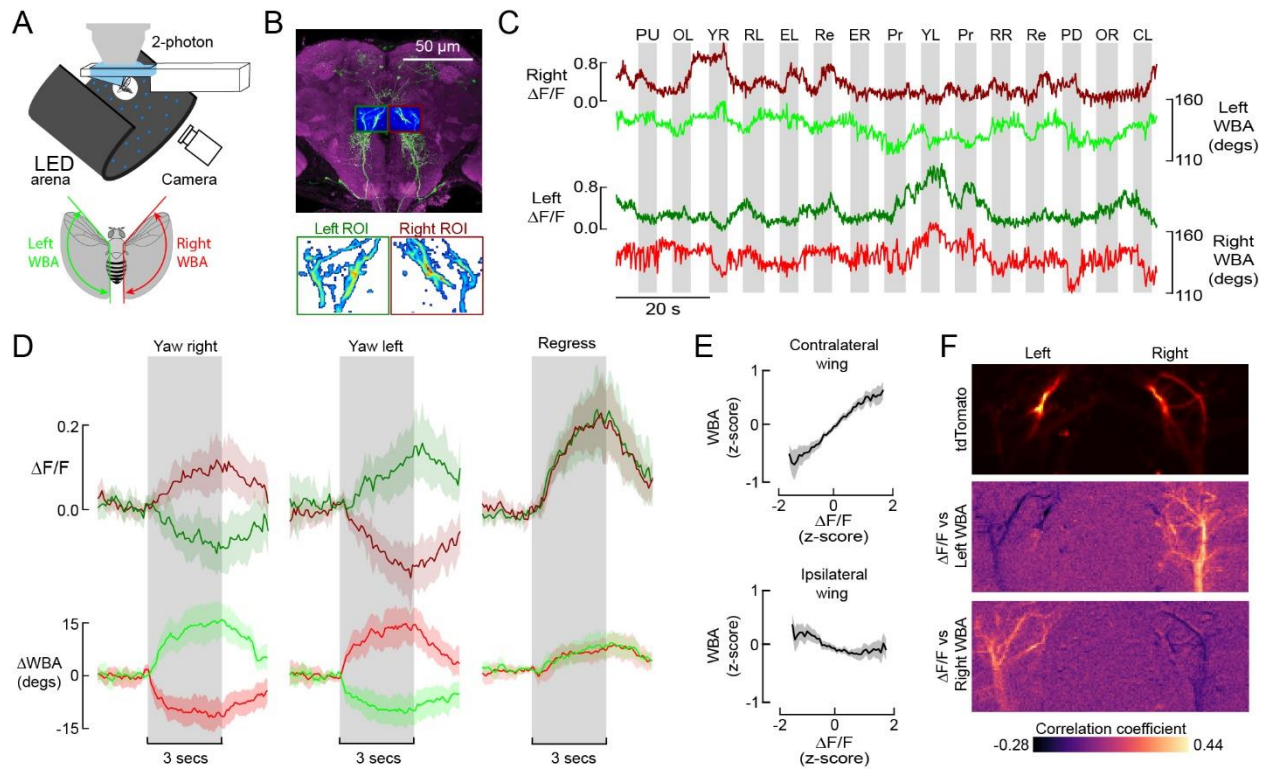
505



506

507 **Figure 3. Wingbeat amplitude appears to be regulated via a population code of DNg02 neurons.** (A) Peak change
 508 in the mean of the left and right WBA elicited by CsChrimson activation in 15 driver lines that target different numbers
 509 of DNg02 neurons; black circle indicates median value for each line, vertical bars indicate interquartile range. The
 510 identity of each line is labeled by vertical text above or below the data. Three sets of lines are plotted close together
 511 because they target the same number of neurons (SS01577, SS02535: 3 cells; SS01578, SS01073: 5 cells; SS01563,
 512 SS02624, SS02625: 8 cells). The number of cell pairs activated positively with the magnitude of the changes
 513 in mean WBA ($r^2 = 0.7394$, based on median values). (B) Time series traces for changes in mean ((left+right)/2)
 514 wingbeat amplitude (top) and frequency (bottom) elicited by optogenetic activation of DNg02 cells in the SS02625 driver
 515 line. Each trace represents the mean response for one fly. Each fly (N=8) is indicated by color, with the variation from
 516 red to black scaled according to the level of background wingbeat frequency. Note that whereas the background, pre-
 517 stimulus wingbeat angle varied among flies, the peak level elicited by CsChrimson activation was quite similar among
 518 flies. Wingbeat frequency also showed a large variation across flies before and after the stimulus, and a decreased
 519 variation during activation. Note that wingbeat frequency tends to fall during optogenetic activation following an initial
 520 rise. (C) Change in wingbeat frequency during optogenetic activation plotted against the pre-stimulus baseline; color
 521 scheme indicates identity of flies plotted in B. Note the inverse relationship; when the background level of wingbeat
 522 frequency is above ~205 Hz, optogenetic activation elicits a drop in frequency below baseline. (H) Wingbeat frequency
 523 plotted against mean ((left+right)/2) wingbeat amplitude for every activation trial of an example fly from panels B and
 524 C. For each trial, the time after stimulus onset is encoded by color; the duration of the stimulus is indicated by the black
 525 bar below the color scale. At stimulus onset, both wingbeat amplitude and frequency rise; however, after WBA reaches
 526 a value of ~160°, further increases in wingbeat amplitude are accompanied by a decrease in wingbeat frequency. The
 527 black curves show isolines for muscle mass specific mechanical power (P^*_{mech}) in the frequency-amplitude plane; see
 528 text for details.

529



530

531 **Figure 4. Left and right DNg02 neurons can act independently to regulate wingbeat amplitude.** (A) Schematic
 532 showing fly tethered to a 2-photon microscope surrounded by an LED array for presentation of visual stimuli and a
 533 camera for tracking wing motion. Inset: a real-time machine vision system tracks wingbeat amplitude (WBA) the left
 534 (green) and right (red) wings of the fly. (B) During functional imaging, we captured DNg02 activity within left (dark green)
 535 and right (dark red) regions of interest, allowing us to measure simultaneous activity across populations of bilateral
 536 cells. The background image is replotted from Figure 2F. Lower inset: within the left and right ROIs, we used a standard
 537 deviation threshold to create a mask within which we measured changes in GCaMP6f fluorescence ($\Delta F/F$) while the
 538 flying fly was subjected to different patterns of visual motion. (C) Example time traces of left and right DNg02 activity
 539 (measured as $\Delta F/F$) along with changes in wingbeat amplitude during presentation of a panel of different visual stimuli
 540 (PU = pattern up, OL = stripe oscillating on right, YR = yaw right, RL = roll left, EL = expansion right, Re = Progressive
 541 motion, YL = yaw left, Pr = progressive motion, YL = yaw left, RR = roll right, PD = pattern down, OR = stripe oscillating
 542 on right, CL = closed loop with stripe). (D) Averaged responses to three most informative patterns of optic flow: yaw
 543 right, yaw left, and regressive motion (N = 20 flies). Top row shows baseline-subtracted $\Delta F/F$ signals from left and right
 544 ROIs (dark green and dark red, respectively). Bottom row shows baseline-subtracted wingbeat amplitude signals for
 545 left and right wings (green and red, respectively). All data are presented as mean (solid line) and a boot-strapped 95%
 546 CI for the mean (shaded area); the 3-second period of stimulus presentation is indicated by the grey patch. (E) Wingbeat
 547 amplitude of the contralateral (top) and ipsilateral (bottom) wing plotted against $\Delta F/F$. Data are derived from two-minute
 548 continuous flight recordings from 20 flies. Both fluorescence and wingbeat signals have been normalized to z-scores;
 549 data are presented as mean (solid line) and a boot-strapped 95% CI for the mean (shaded area). (F) Correlation
 550 between GCaMP6f fluorescence and wingbeat amplitude plotted on a pixel-by-pixel basis within the recording ROI.
 551 The top image shows the expression pattern of tdTomato in the ROI of an example fly. The middle image shows the
 552 pixel-by-pixel correlation of the $\Delta F/F$ signal with left wingbeat amplitude recorded over a 2-minute flight bout; the bottom
 553 image shows the corresponding pixel-by-pixel correlation for right wingbeat amplitude. Note that activity in the DNg02
 554 cells are positively correlated with wingbeat amplitude in the contralateral wing and negatively correlated with wingbeat
 555 amplitude of the ipsilateral wing.

556